

Electronic Supplementary Information

High ionic conductivity and toughness hydrogel electrolyte for high-performance flexible solid-state zinc-ion hybrid supercapacitors enabled by cellulose-bentonite coordination interactions

Jie Lu,^a Xiangyu Lin,^b Siheng Wang,^b Xu Xu^c, Yiyang Zhou,^a Yashu Zhang,^a Qingtao Li ^{*a}
and He Liu ^{*b}

^a College of Light Industry and Food Engineering, Guangxi University, Nanning 530004, Guangxi Zhuang Autonomous Region, China.

^b Institute of Chemical Industry of Forestry Products, Chinese Academy of Forestry, Key Laboratory of Biomass Energy and Material, Key Lab. of Chemical Engineering of Forest Products, National Forestry and Grassland Administration, National Engineering Laboratory for Biomass Chemical Utilization, Nanjing 210042, Jiangsu Province, China.

^c Jiangsu Co-Innovation Center of Efficient Processing and Utilization of Forest Resources, College of Chemical Engineering, Nanjing Forestry University, Nanjing 210037, Jiangsu Province, China.

* Corresponding authors. Email: lqt2222@163.com (Q. L.), liuhe.caf@gmail.com (H. L.)

Content of Supporting Information

Section S1 Experimental Section

Section S2 Characterization of cellulose, BT, and the CBH-Zn

Section S3 Mechanical performance of the CH, CBH, CH-Zn, and CBH-Zn

Section S4 Anti-freezing property and ionic conductivity

Section S5 Electrochemical performance of the zinc-ion hybrid capacitors

Section S6 Application of the integrated systems

Section S7 Tables

Section S8 References

Movie S1

The integrated system was tied to different parts of the human body, and the CBH-ZHSC used the electrical energy provided by solar cells to power the appliances.

Section S1 Experimental Section

Materials: Zinc sulfate heptahydrate ($\text{ZnSO}_4 \cdot 7\text{H}_2\text{O}$), sodium hydroxide (NaOH), and urea were supplied by Aladdin Chemical Reagent Co., Ltd. 1, 4-butanediol diglycidyl ether (BDE) was supplied by Guangdong Weng Jiang Chemical Reagent Co., Ltd. Bentonite was purchased from Shenzhen Jintenglong Industrial Co., Ltd. Activated carbon (SSA: $\sim 1800 \text{ m}^2 \text{ g}^{-1}$) was gained from XFNANO Materials Tech Co., Ltd. All chemicals were analytical grade.

Extraction of biomass cellulose: The biomass cellulose was prepared by soaking poplar powder in an alkaline solution to remove lignin, hemicellulose, and other components.¹ Firstly, the raw cellulose fiber was prepared by adding a certain amount of poplar powder into 5 wt% NaOH solution and stirring at 70 °C for 4 h, followed by repeated washing with DI water and ethanol in turn. Then, the above raw cellulose fiber was immersed in a mixture of sodium chloride (2 wt%) and acetic acid, and subsequently stirred at 60 °C for 4 h to obtain a white cellulose suspension which was washed to neutral with DI water. Finally, cellulose pulp was produced by drying in a vacuum oven at 60 °C for 12 h.

Preparation of the CBH-Zn: The cellulose pulp (3 g) was dissolved in 97 g of the mixed solvent of NaOH, urea, and DI water (weight ratio = 7: 12: 81) at -12 °C to prepare the cellulose solution (3 wt%), which was determined by the previous report.² Under stirring, BT powder (0.3 g) and chemical cross-linker BDE (0.75 g) were slowly mixed into the above cellulose solution. The resultant solution was degassed and poured into the mold and cured in a water bath kettle at 60 °C for 2 h to form a gel. The CBH-Zn was obtained by immersing the above hydrogel in DI water for 3 days and then soaking it in an aqueous 2.0 M ZnSO_4 solution for 48 h. The detailed composition of all the research samples was enumerated in Table S4.

Characterizations: The three-dimensional structure of the hydrogel stained with fluorescent dye solution was observed by confocal laser scanning microscopy (CLSM) (LSM710, Zeiss, Germany). Environmental scanning electron microscopy (JSM-7600 Fs, JEOL, Japan) was used to analyze the morphology and microstructure of the CBH-Zn, and the elemental composition was studied by energy dispersive X-ray spectroscopy (EDS). The microstructure of BT was characterized by field emission scanning electron microscopy (FESEM) (Regulus

8100, Hitachi, Japan) and transmission electron microscopy (TEM) (JEM-2100 UHR, JEOL, Japan). The X-ray diffraction (XRD) patterns of the cellulose, BT, and freeze-dried CBH-Zn in the diffraction angle (2θ) range from 3° to 70° were conducted by Ultima IV-ray diffractometer (Rigaku, Japan) with a scanning speed of 5° min^{-1} . The Fourier transform infrared (FTIR) spectra of cellulose, BT, and the freeze-dried CBH-Zn were characterized by Fourier transform infrared spectrometer (Nicolet iS50, Thermo Fisher Scientific, USA) with a wavelength range from 4000 cm^{-1} to 400 cm^{-1} . The chemical composition and elemental bond energy changes of the CBH-Zn were analyzed by X-ray photoelectron spectroscopy (XPS) (Kratos Axis Ultra DLD, KRATOS, UK). The freezing point of the CBH-Zn was examined by differential scanning calorimetry (DSC) (PerkinElmer Diamond, PerkinElmer, USA) at a cooling/heating rate of $5^\circ \text{ C min}^{-1}$ from -40° C to 30° C .

Mechanical measurements: Compression tests were measured by the versatile testing machine with a 5000 N load sensor (UTM6503, Shenzhen SANS Testing Machine Co. Ltd., China) at a constant loading and unloading speed of 2 mm min^{-1} . Three specimens were made for each sample (height of 10 mm, diameter of 10 mm) and mean values were reported. Cyclic compression tests were performed with no time interval between two cycles. According to the slope of elastic strain region of the compressive stress-strain curve, compressive modulus of the hydrogel was calculated.

Conductivity of the cellulose hydrogel electrolyte: The electrochemical workstation (CHI 660D, Chenhua, China) determined the ionic conductivity of hydrogels by EIS at frequencies from 0.1 Hz to 100 kHz and the voltage of 0.1 V. Hydrogels, which were soaked in different concentrations of an aqueous ZnSO_4 solution, different immersion times, and different temperatures, were sandwiched between two nickel sheets for the measurement. The ionic conductivity of the hydrogels was calculated according to the following Equation:

$$\sigma = \frac{L}{A \times R} \quad (1)$$

where L (cm), A (cm^2), and R (Ω) represent the distance between adjacent nickel sheets, the cross-sectional area and the electrical resistance of the hydrogel.

Evaluation of water retention capacity: The water retention of hydrogel samples (10 mm in diameter and 10 mm in height) were evaluated by following equation at a relative humidity

(RH) of 50% and a temperature of 25 °C:

$$\text{Weight ratio} = \frac{W_i}{W_o} \quad (2)$$

where W_i and W_o are the weight of the hydrogel at time i and the initial weight of the hydrogel, respectively.

Electrochemical measurements: For the ZHSC, cathode slurry was prepared by mixing the active material (AC), conductive agent (carbon black), and binder (polyvinylidene fluoride (PVDF)) at a weight ratio of 8: 1: 1 in 1-methyl-2-pyrrolidone solvent, and then coating the mixture onto the titanium foil. The electrode was dried in a vacuum at 80 °C for 24 h (the mass loading of the active material was 1.0–1.2 mg cm⁻²). Zn foil was considered as the anode, which should be polished with fine-grained sandpaper before use to avoid oxidation. The flexible CBH-ZHSC was composed of Zn anode, CBH-Zn, and AC cathode. Electrochemical performance of the ZHSC, such as cyclic voltammetry (CV), galvanostatic charge-discharge (GCD), and electrochemical impedance spectroscopy (EIS), was tested by the CHI660D electrochemical workstation. The CV test was carried out within the voltage range of 0.2-1.8 V, and the scan rate was between 3 mV s⁻¹ and 50 mV s⁻¹. The GCD curve was obtained with the current density ranging from 0.5 A g⁻¹ to 20.0 A g⁻¹. The EIS test was performed in the frequency range from 0.01 Hz to 100 kHz. Moreover, the cycling stability of the CBH-ZHSC was measured on a LAND CT3001AU battery-testing instrument (LANHE, China) with a charge/discharge rate of 10.0 A g⁻¹ for 45000 cycles. To contrast the effect of BT doping on the electrochemical performance of the CBH-ZHSC, Zn//CH-Zn//AC ZHSC (CH-ZHSC) was assembled. The value of the specific capacitance C (F g⁻¹) was calculated from the GCD curves according to the following Equation:

$$C = \frac{I \times \Delta t}{m \times U} \quad (3)$$

where I (A), Δt (s), m (g), and U (V) are the constant discharge current, discharge time, mass of the active material, and change in potential during the discharge (removing the IR drop), respectively.

The energy density E (Wh kg⁻¹) and power density P (W kg⁻¹) of the CBH-ZHSC were determined according to Equation (4) and Equation (5):

$$E = \frac{C \times V^2}{2 \times 3.6} \quad (4)$$

$$P = \frac{E \times 3600}{\Delta t} \quad (5)$$

where V (V) manifests the discharge voltage range.

Section S2 Characterization of cellulose, BT, and the CBH-Zn

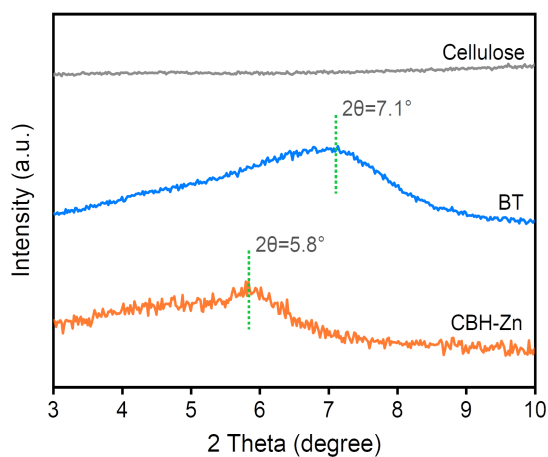


Figure S1. XRD patterns of the cellulose, BT, and the CBH-Zn.

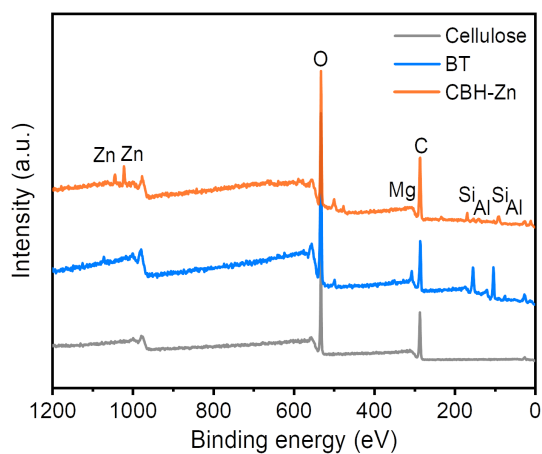


Figure S2. XPS spectrum of cellulose, BT, and CBH-Zn. The XPS spectrum of the CBH-Zn showed that BT and $\text{ZnSO}_4 \cdot 7\text{H}_2\text{O}$ were successfully introduced into the nanocomposite hydrogel.

Section S3 Mechanical performance of the CH, CBH, CH-Zn, and CBH-Zn

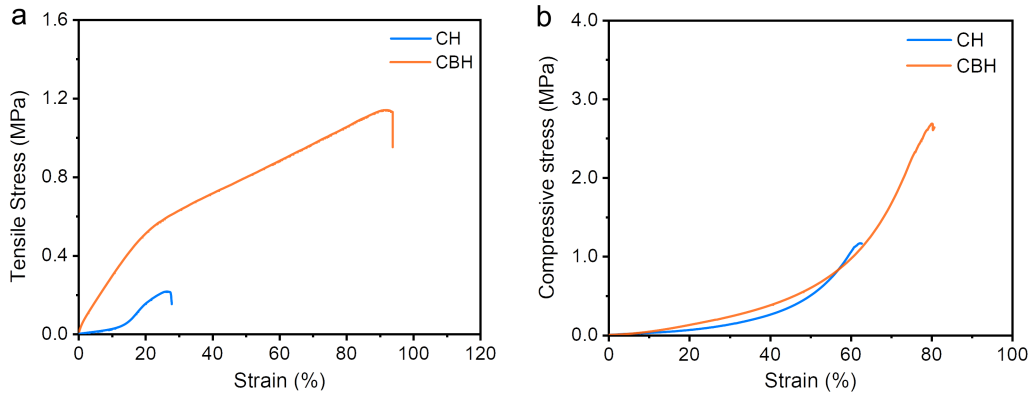


Figure S3. (a, b) Tensile stress-strain curves (a) and compressive stress-strain curves (b) of the CH and CBH. The tensile fracture stress and strain of the CH were 0.21 MPa and 27.6%, and the maximum compressive stress and fracture strain were 1.16 MPa and 62.5%, respectively. The tensile fracture stress and strain of the CBH were 1.14 MPa and 93.9%, and the maximum compressive stress and fracture strain were 2.67 MPa and 80.1%, respectively. The coordination interaction between the cellulose and BT nanoplatelets made the cellulose hydrogels doped with BT possessed excellent mechanical properties.

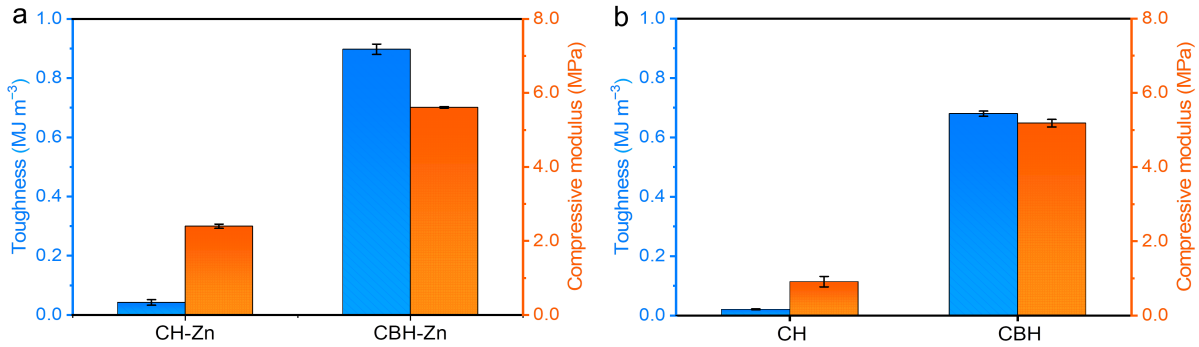


Figure S4. (a, b) Compressive modulus and fracture energy of the cellulose hydrogels containing ZnSO₄ (a) and without ZnSO₄ (b). The compressive modulus and fracture energy of the CH and CH-Zn were 0.9 MPa, 0.02 MJ m⁻³ and 2.4 MPa, 0.04 MJ m⁻³, respectively. The introduction of BT nanoplatelets enhanced the compressive modulus and fracture energy of the CBH and CBH-Zn to 5.2 MPa, 0.68 MJ m⁻³ and 5.6 MPa, 0.90 MJ m⁻³, respectively. The results demonstrated the BT could boost the strength and toughness of the cellulose hydrogels.

Section S4 Anti-freezing property and ionic conductivity

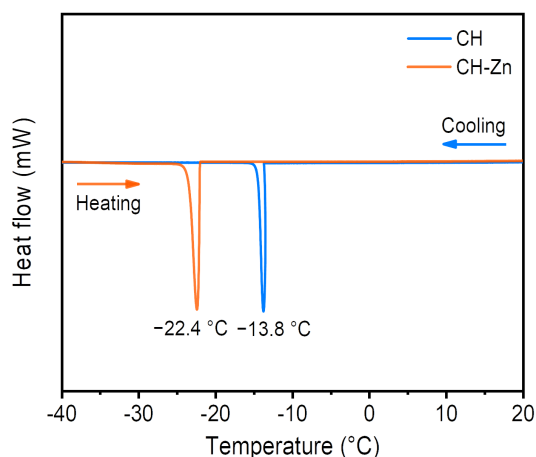


Figure S5. DSC curves of the CH and CH-Zn. After the CH was soaked in an aqueous 2.0 M ZnSO₄ solution, freezing point decreased from -13.8 °C to -22.4 °C due to the formation of salt/water system in the hydrogel, which broke the hydrogen bond between water molecules.

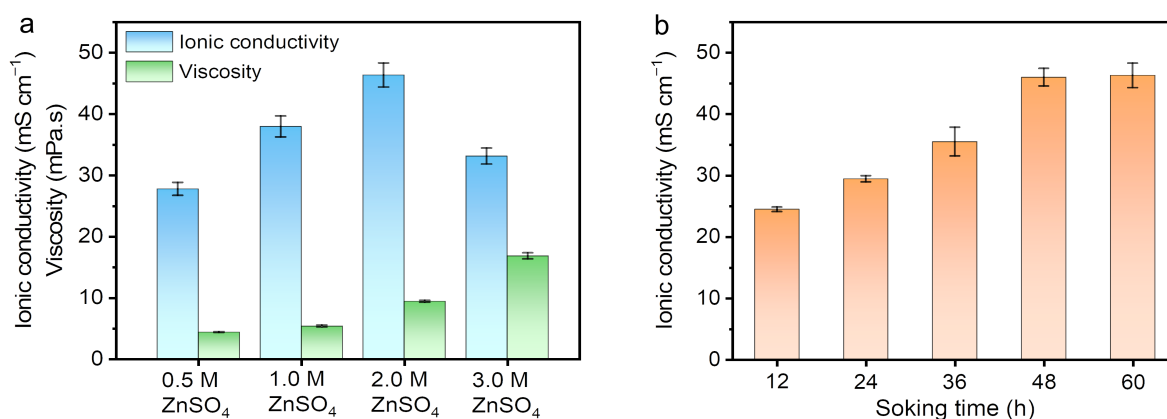


Figure S6. (a) Viscosity and ionic conductivity of aqueous ZnSO₄ solution electrolytes with different concentrations. (b) Ionic conductivity of the CBH soaked in an aqueous 2.0 M ZnSO₄ solution for different periods.

Fig. S6a investigated the ionic conductivity and viscosity of the ZnSO₄ electrolytes with different concentrations (0.5, 1.0, 2.0, and 3.0 M). It was found that with the concentration increasing from 0.5 M to 3.0 M, the viscosity enhanced from 4.3 mPa·s to 16.8 mPa·s while the ionic conductivity added from 27.7 mS cm⁻¹ in 0.5 M ZnSO₄ to the highest value of 46.3 mS cm⁻¹ in 2.0 M ZnSO₄, whereas decreased to 33.1 mS cm⁻¹ in 3.0 M ZnSO₄. This was due to the high viscosity of the concentrated ZnSO₄ would retard the ion transport and reduce the ionic conductivity.³ Therefore, 2.0 M ZnSO₄ with the first-rank ionic conductivity was

selected as the electrolyte for the preparation of ionic conductive hydrogel. As shown in Fig. S6b, the CBH was soaked in an aqueous 2.0 M ZnSO₄ solution to explore the effect of different soaking time on ionic conductivity of the hydrogels. Results showed that ionic conductivity of the CBH-Zn improved with the increase of times, and remained almost constant after 48 h. Therefore, the ionic conductivity was measured by soaking the hydrogel in an aqueous 2.0 M ZnSO₄ solution for 48 h.

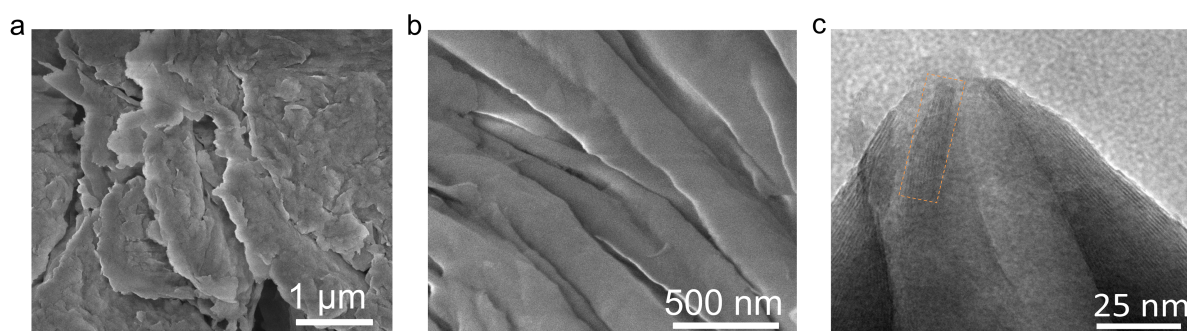


Figure S7. (a-c) SEM (a), magnified SEM (b), and TEM (c) images exhibit the lamellar structure of BT, which is conducive to the ion storage and migration.

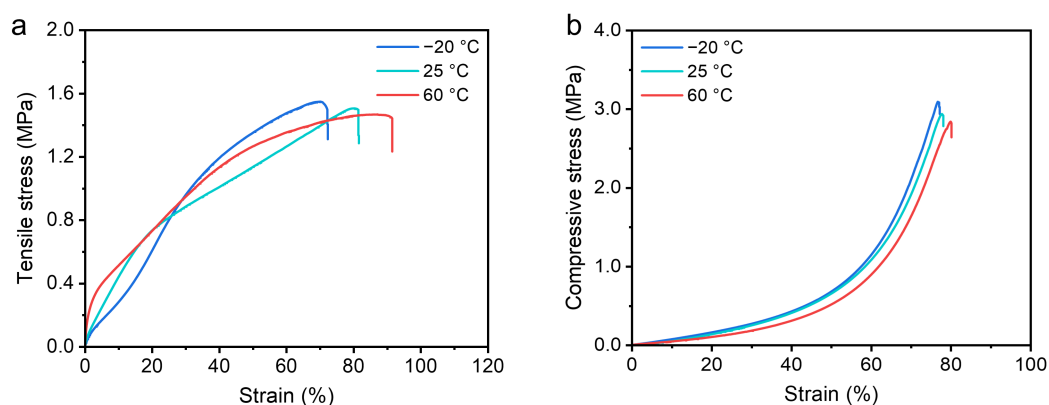


Figure S8. (a, b) Tensile stress-strain curves (a) and compressive stress-strain curves (b) of the CBH-Zn under different temperatures. The tensile fracture stress of the CBH-Zn at 60 °C and -20 °C was 1.46 and 1.54 MPa with the fracture strain of 92% and 73%, respectively, presenting no significant changes compared to the CBH-Zn at 25 °C. In addition, the maximum compressive stresses of the CBH-Zn at 60 °C, 25 °C, and -20 °C were 2.83, 2.93, and 3.07 MPa with the fracture strain of 80%, 78%, and 77%, respectively, exhibiting no

significant difference.

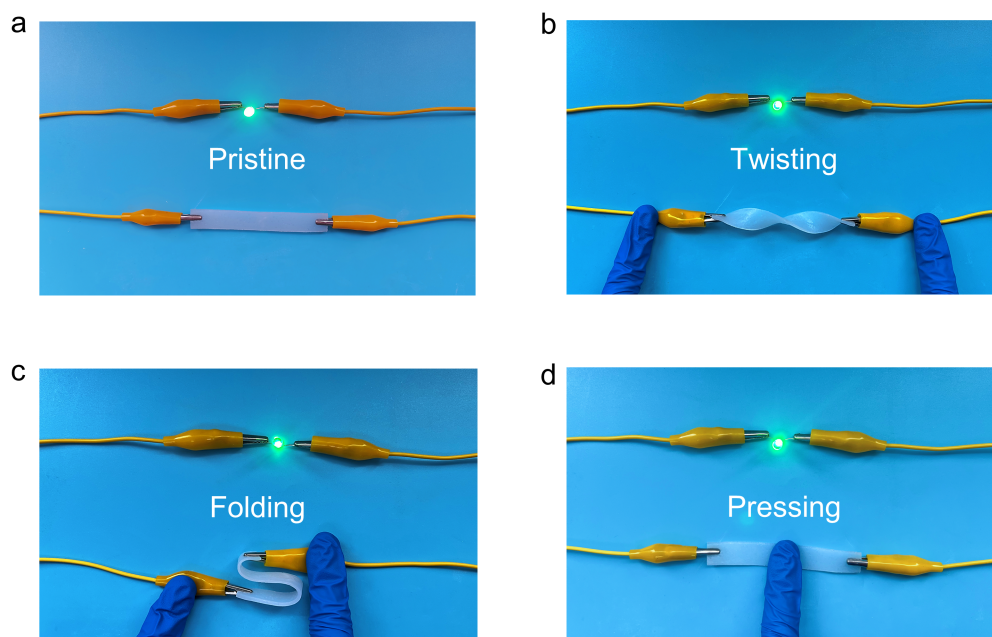


Figure S9. Effect of the CBH-Zn on LED lamp brightness in original, twisted, folded and pressed states.

Section S5 Electrochemical performance of the zinc-ion hybrid capacitors

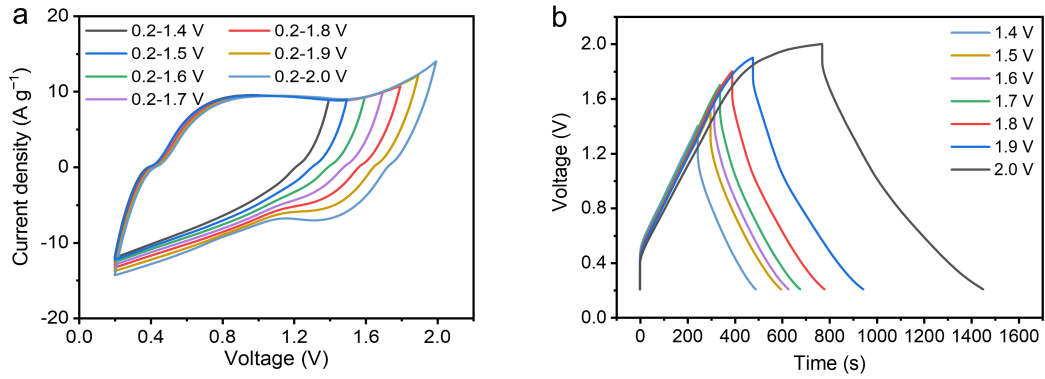


Figure S10. (a) CV curves of the CBH-ZHSC at 50 mV s⁻¹. (b) GCD curves of the CBH-ZHSC at 1.0 A g⁻¹.

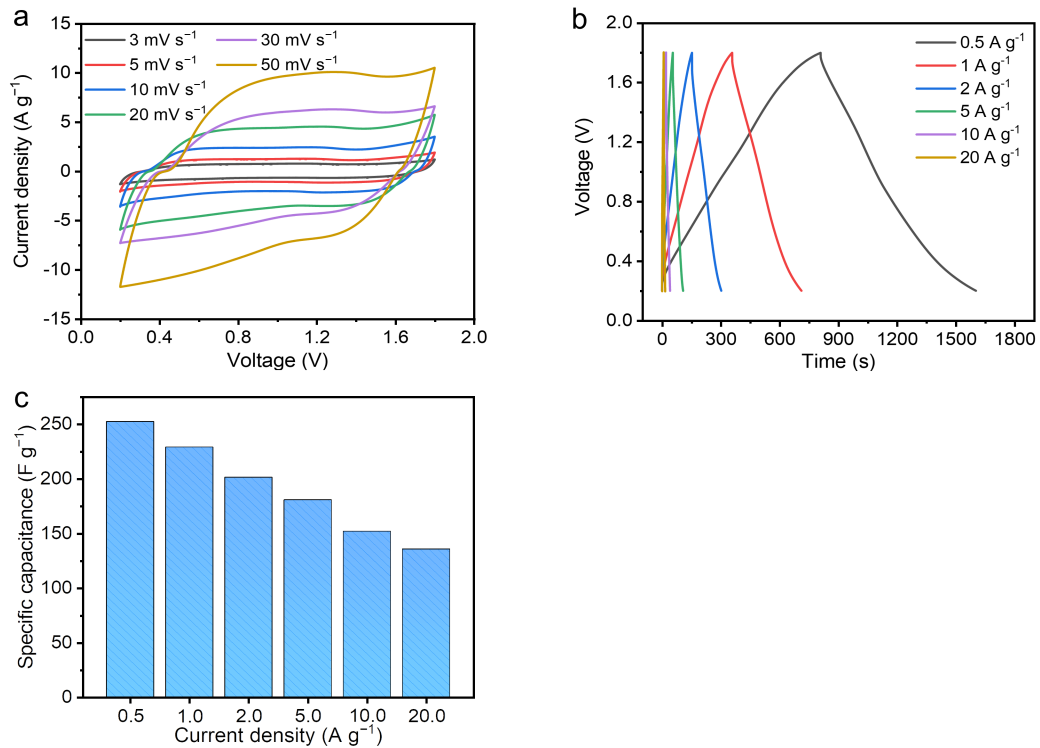


Figure S11. (a, b) CV curves of the aqueous ZHSC at different scan rates (a) and GCD curves at different current densities (b) in a working voltage range of 0.2–1.8 V. (c) Specific capacitance of the aqueous ZHSC at different current densities. After determining the stable operating voltage range of 0.2–1.8 V for the CBH-ZHSC, the electrochemical behavior was investigated by CV at different scan rates. The CV curve did not exhibit significant deformation even at a high scan rate of 50 mV s⁻¹, implying the aqueous ZHSC possessed

excellent reversibility and rapid electrochemical reactions. The GCD curves of the aqueous ZHSC at different current densities were almost symmetry, indicating the ZHSC had excellent electrochemical reversibility under the potential window from 0.2 V to 1.8 V. The specific capacitances at current densities of 0.5 A g⁻¹, 1.0 A g⁻¹, 2.0 A g⁻¹, 5.0 A g⁻¹, 10.0 A g⁻¹, and 20.0 A g⁻¹ were 252.6 F g⁻¹, 229.2 F g⁻¹, 201.5 F g⁻¹, 181.0 F g⁻¹, 152.0 F g⁻¹, and 135.8 F g⁻¹.

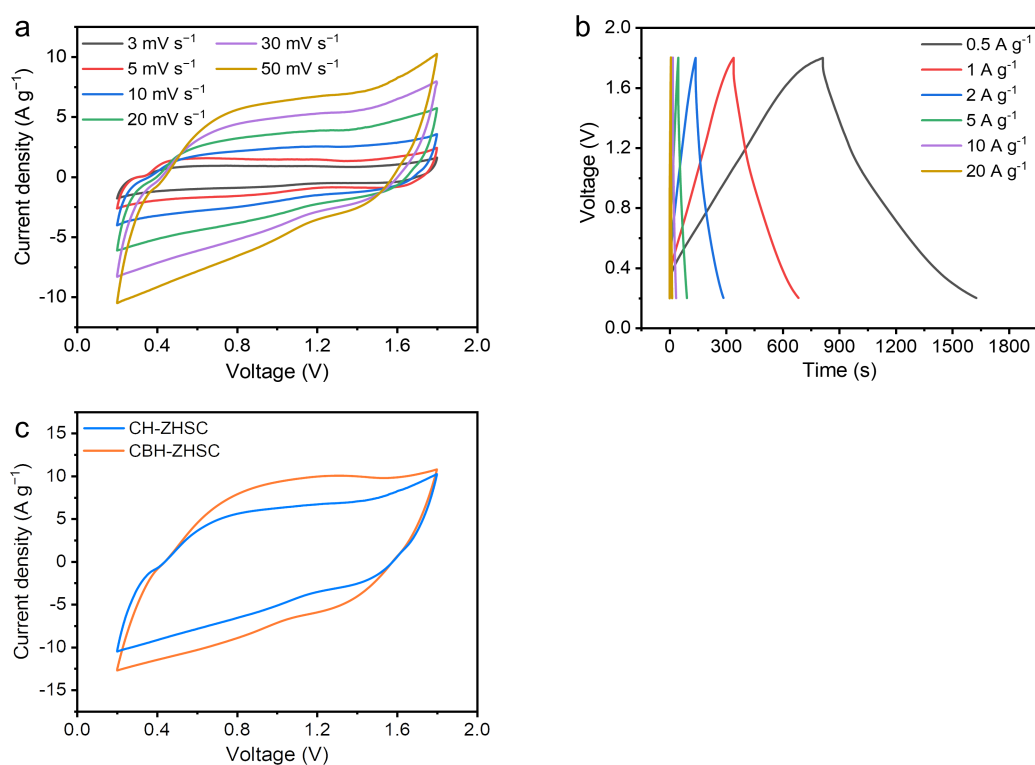


Figure. S12. (a, b) CV curves of the CH-ZHSC at different scan rates (a) and GCD curves at different current densities (b) in a working voltage range of 0.2–1.8 V. (c) CV curves of the CH-ZHSC and CBH-ZHSC at a scan rate of 50 mV s⁻¹. The specific capacitance of the CH-ZHSC was 264.0 F g⁻¹, 215.1 F g⁻¹, 202.5 F g⁻¹, 175.9 F g⁻¹, 134.6 F g⁻¹, and 126.9 F g⁻¹ when the current densities were 0.5 A g⁻¹, 1.0 A g⁻¹, 2.0 A g⁻¹, 5.0 A g⁻¹, 10.0 A g⁻¹, and 20.0 A g⁻¹, which was calculated by GCD curves according to Equation (3). By comparing the CV curves of the CH-ZHSC and CBH-ZHSC at 50 mV s⁻¹, the CV area of the CBH-ZHSC was higher than the CH-ZHSC, indicating that the doping of BT into the cellulose hydrogel electrolytes could improve electrochemical performance of the ZHSC.

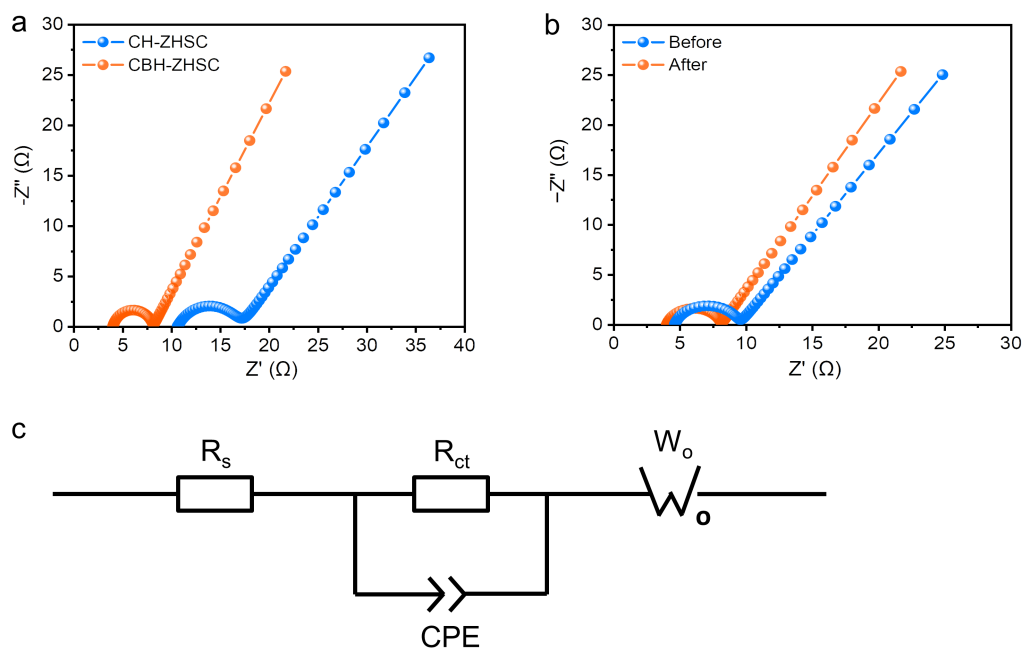


Figure S13. (a) Nyquist plots of the CH-ZHSC and CBH-ZHSC. (b) Nyquist plots of the CBH-ZHSC before and after charge/discharge cycle measurement. (c) Fitting equivalent analogue circuit of the CH-ZHSC and CBH-ZHSC.

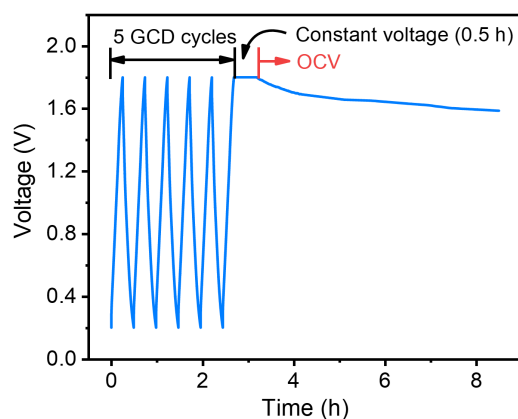


Figure S14. Illustration of the self-discharge behavior test. The CBH-ZHSC was charged/discharged through GCD technique at 0.5 A g^{-1} for 5 cycles, and then maintained at the expected voltage for 30 minutes by constant voltage charging technique, which was used to achieve a relatively stable internal environment of electrochemical devices.

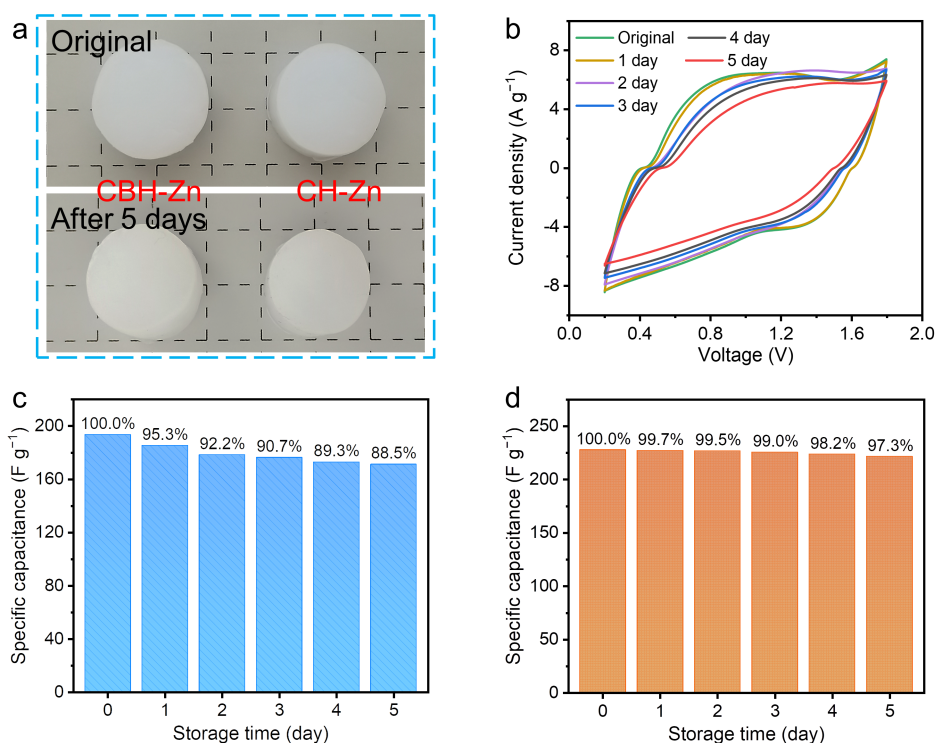


Figure S15. (a) Pictures of the hydrogel electrolytes before and after 5 days of placement. (b) CV curves of the CH-Zn at 50 mV s⁻¹ for different storage days. (c, d) Specific capacitance of the CH-ZHSC (c) and CBH-ZHSC (d) after being placed for different days. The area of CV curves of the CH-ZHSC after storage for different days changed greatly, indicating that the electrochemical performance of the CH-ZHSC decreased obviously. Compared with the CH-ZHSC, CBH-ZHSC exhibited a high capacity retention of 97.3% after 5 days of storage at room temperature, manifesting that the addition of BT nanoplatelets with water retention capacity could effectively inhibit the evaporation of water in the hydrogel electrolyte, making the CBH-ZHSC possessed outstanding electrochemical performance.

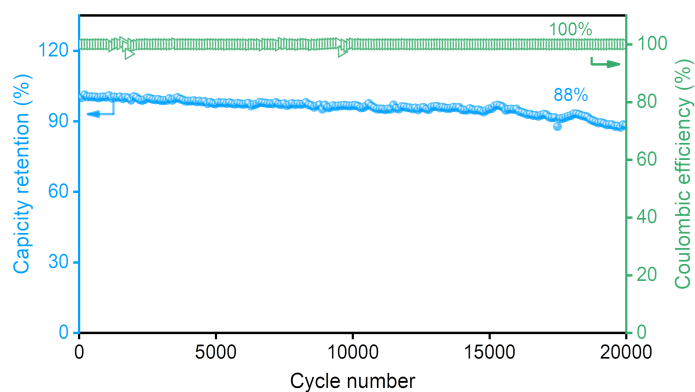


Figure S16. The capacity retention and coulombic efficiency of the CH-ZHSC were 88% and

100%, after 10000 charge/discharge cycles at current density of 10.0 A g⁻¹.

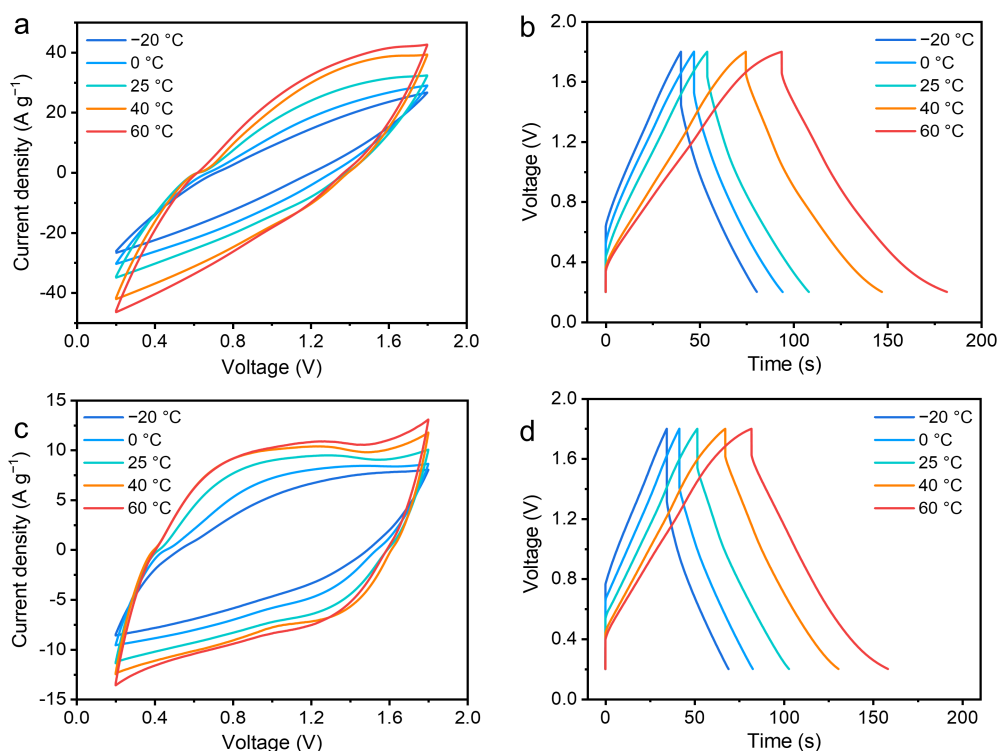


Figure S17. (a, b) CV curves at 50 mV s⁻¹ (a) and GCD curves at 5.0 A g⁻¹ (b) of the CBH-ZHSC under different operation temperatures. (c, d) CV curves at 50 mV s⁻¹ (c) and GCD curves at 5.0 A g⁻¹ (d) of the CH-ZHSC under different operation temperatures. The decrease area of CV curves of the CH-ZHSC and CBH-ZHSC were due to the decrease of ion diffusion kinetics with the decline of temperature. The area of the CBH-ZHSC was higher than that of the CH-ZHSC, indicating that the CBH-ZHSC possessed satisfactory electrochemical performance. By comparing the discharge time of the CH-ZHSC and CBH-ZHSC at different temperatures, it could be further proved that the addition of BT nanoplatelets made the ZHSC exhibit excellent electrochemical properties.

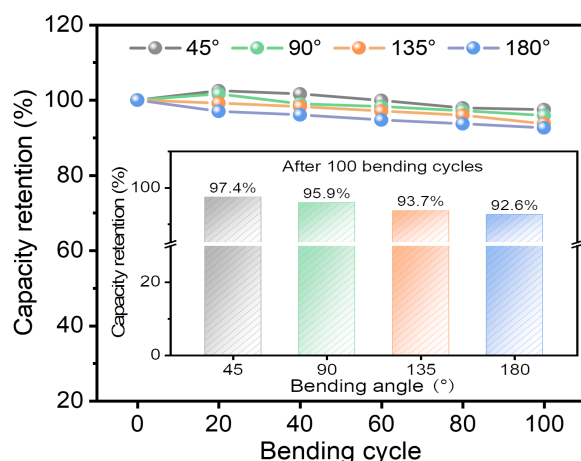


Figure S18. Capacity retention of the CBH-ZHSC under different bending angles and cycles. The electrochemical workstation was used to charge/discharge the CBH-ZHSC, and capacity retention of the CBH-ZHSC was calculated after bending 100 times. When the bending angle was less than 90°, capacity retention reached 97.4% after 100 bending cycles. When the bending angle was increased to 90° or above, the prolongation of ion transport path in the CBH-Zn decreased the ion conductivity. Therefore, electrochemical stability of the CBH-ZHSC decreased slightly, whereas maintained a high level. When the bending angle was 180°, the capacity retention of the CBH-ZHSC was 92.6% after 100 cycles of continuous bending, indicating its excellent characteristics in flexibility and high energy storage performance.

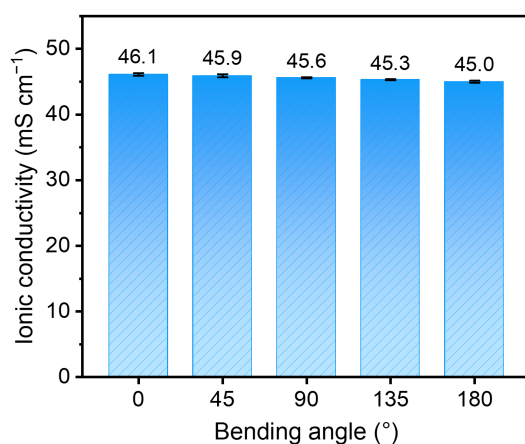


Figure S19. Ionic conductivity of the CBH-Zn electrolyte under different bending angles. The electrochemical workstation was used to analyze the ionic conductivity of the CBH-Zn after 100 consecutive bending cycles at different bending angles. The ionic conductivity still remains at a high level, regardless of the slightly decreased ionic conductivity caused by the

prolongation of the ion transport path inside the CBH-Zn along with the increased bending angles. When the CBH-Zn was bent to 180° and repeated for 100 cycles, the ionic conductivity of the CBH-Zn just exhibited a slight decrease of 2.4%.

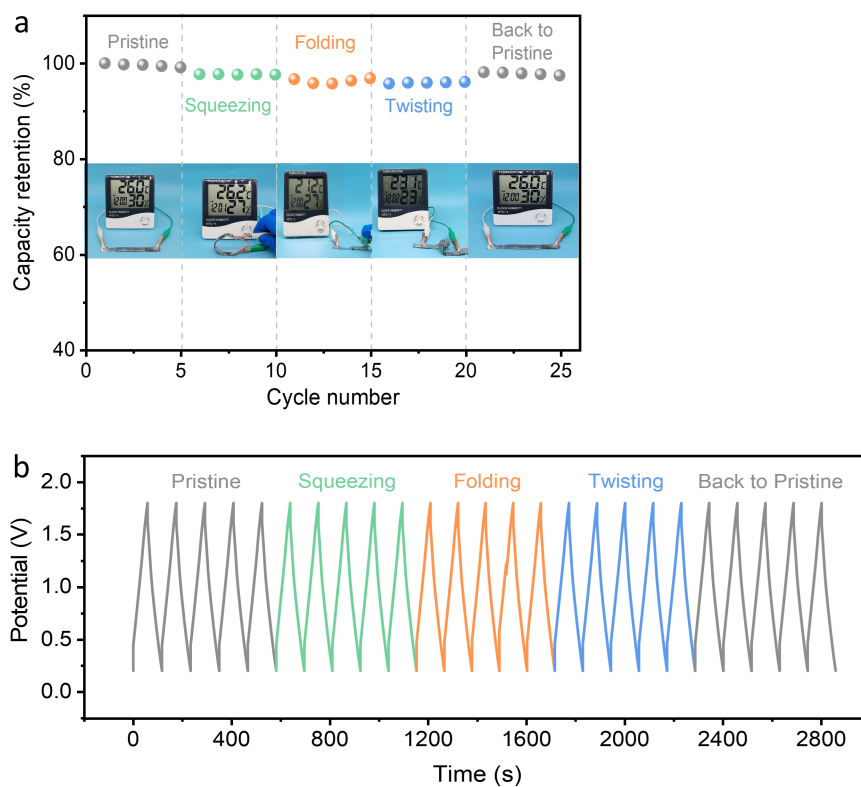


Figure S20. (a) Capacity retention of the CBH-ZHSC under different dynamic deformation conditions, and the illustration showed the diagram of the CBH-ZHSC powering a timer under the corresponding dynamic deformation conditions. (b) GCD curves of the CBH-ZHSC under various dynamic deformations at 5.0 A g⁻¹.

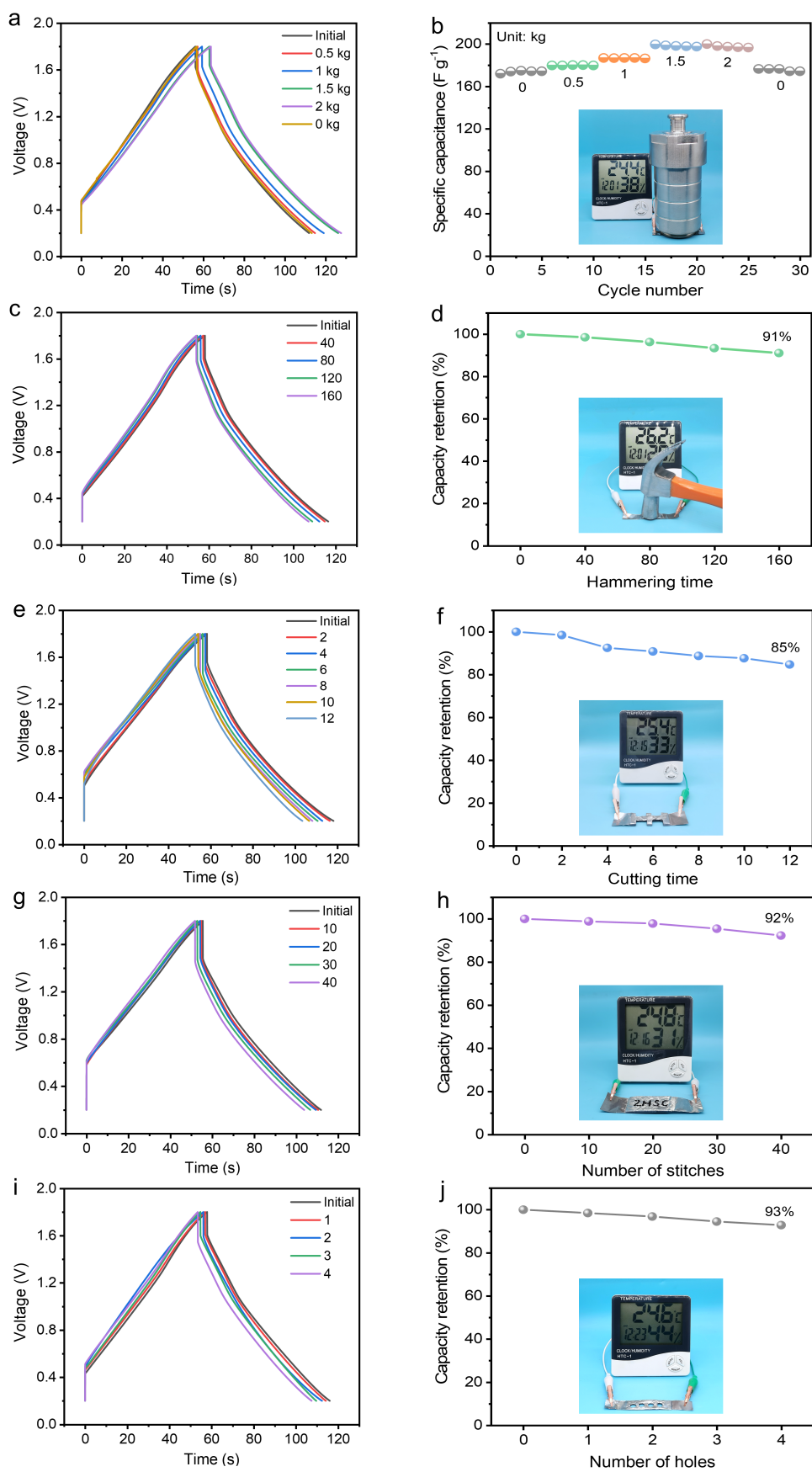


Figure S21. (a, b) GCD ($5.0 A g^{-1}$) curves (a) and capacity retention (b) of the CBH-ZHSC

under different heavy loads. The CBH-ZHSC had a slight increase in specific capacitance when loaded with heavy loads, which may be caused by shortening the ion transport path in the electrolyte under high loading. The excellent mechanical properties of the CBH-ZHSC prevent it from short-circuiting at higher loads. (c, d) GCD (5.0 A g^{-1}) curves (c) and capacity retention (d) of the CBH-ZHSC at different hammering times. After 160 times hammer strikes, the capacity retention of the CBH-ZHSC maintains 91% and could drive the electronic watch to work stably, which was due to the high mechanical strength of the CBH-Zn reduced the mechanical impact of the CBH-ZHSC. (e-j) GCD (5.0 A g^{-1}) curves and capacity retention of the CBH-ZHSC at different cutting cycles (e, f), sewing cycles (g, h), and punching cycles (i, j). The capacity retention of CBH-ZHSC was 85%, 92%, and 93% after 12 cycles cutting, 40 cycles sewing, and 4 cycles punching, and the electronic watch could still work continuously and stably without short circuit phenomenon, which further proved satisfactory mechanical properties of the CBH-Zn.

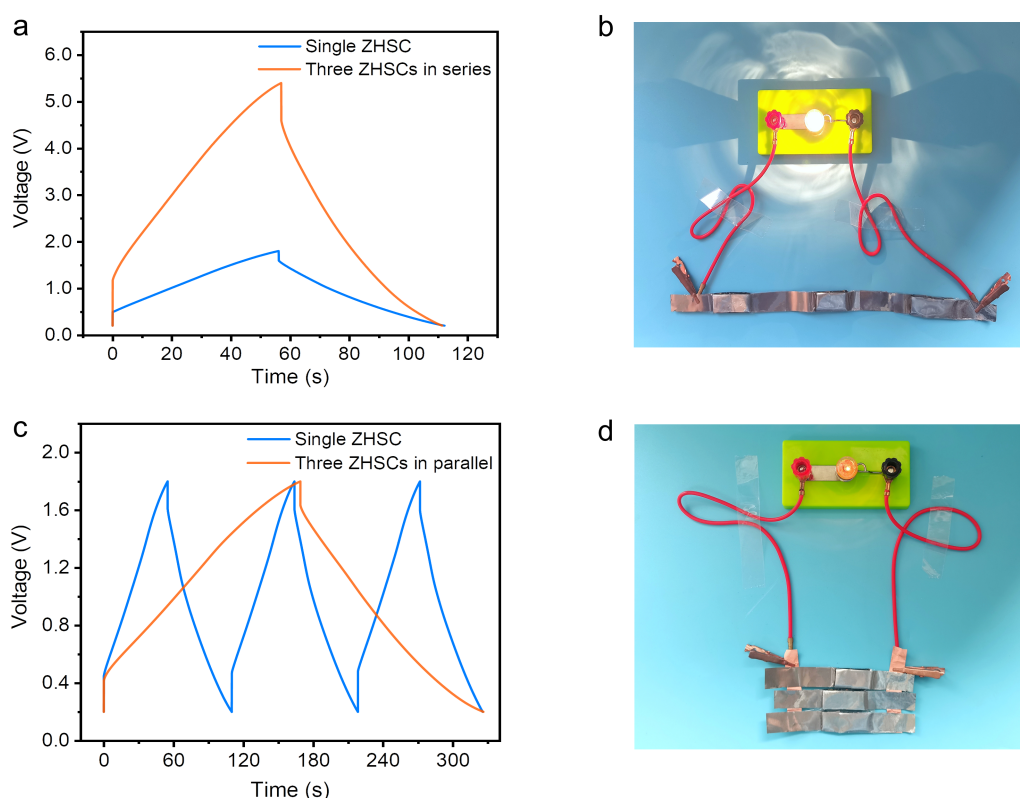


Figure S22. (a) GCD (5.0 A g^{-1}) curves of the single and three-in-series CBH-ZHSCs. (b) Bulbs powered by three-in-series CBH-ZHSCs. (c) GCD (5.0 A g^{-1}) curves of the single and

three CBH-ZHSCs connected in parallel. (d) Bulbs powered by three CBH-ZHSCs connected in parallel.

Compared with the maximum working voltage of 1.8 V for a single CBH-ZHSC, three CBH-ZHSCs in series could increase the voltage to 5.4 V. Furthermore, the discharge time of three CBH-ZHSCs in parallel was three times longer than that of single CBH-ZHSC. The three CBH-ZHSCs in series or parallel could light the bulb, which was brighter due to the higher working voltage of the CBH-ZHSC in series.

Section S6 Application of the integrated systems

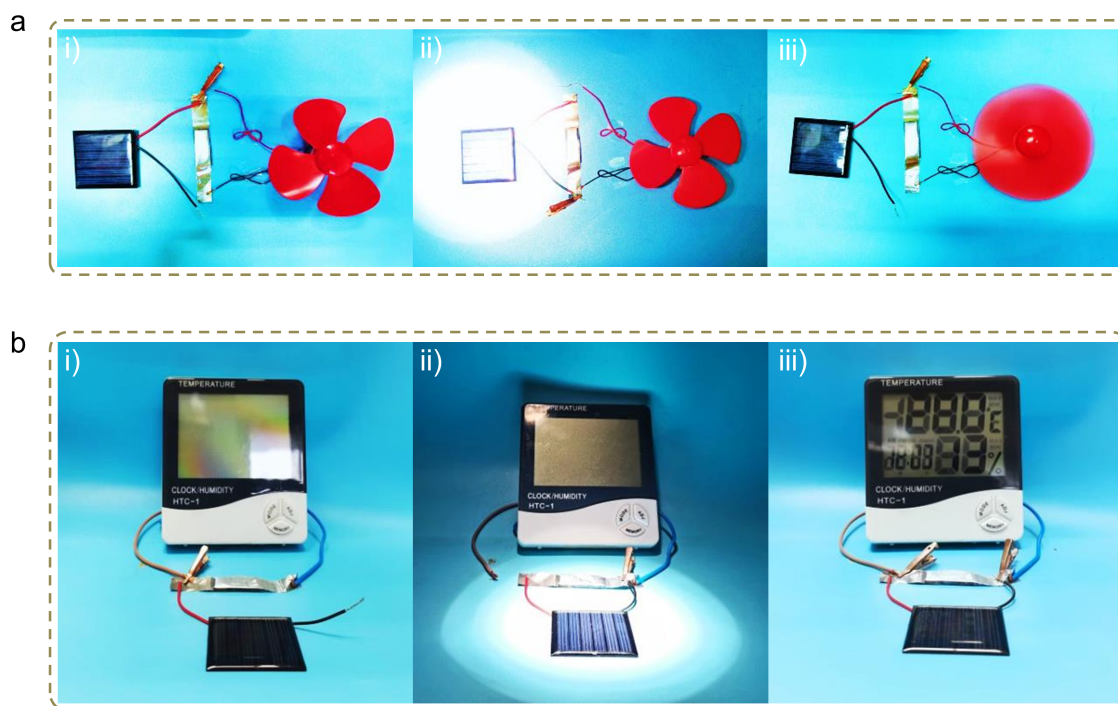


Figure S23. The solar cell converted light energy into electrical energy stored in the CBH-ZHSC. (a, b) Fans (a) and electronic watches (b) worked by utilizing the electrical energy stored in the CBH-ZHSC.

Section S7 Tables

Table S1 Composition of the mechanical properties and ionic conductivity of the CBH-Zn with those reported hydrogel electrolytes.

Hydrogels	Tensile strength (kPa)	Compressive strength (kPa)	Ionic conductivity (mS cm ⁻¹)	Refs.
CBH-Zn	1510.00	2930.00	46.30	This work
PVA/NFC/ZnSO ₄	23.13	26.20	18.10	4
TC-7.5/PSA	103.70	1600.00	74.30	5
XG-PAM/CNF	84.00	350.00	28.8	6
Cellulose	370.00	—	74.90	7
Sor-Cel	620.00	—	35.40	8
CNF-PAM	192.00	—	6.80	9
PAAm-PVP/LiCl	220.00	210.00	20.00	10
SPMA-Zn	58.00	700.00	73.50	11
κ -CG/ PAAm/Zn(CF ₃ SO ₃) ₂	34.60	75.30	23.00	12
PAA-g-EG _{50%} /KOH	253.22	—	6.28	13
HIWW	420.00	—	4.20	14
SPI-PAAm	—	1500.00	16.34	15
PAAm/gelatin	138.00	1360.00	40	16
PolySH/LiCl	5.00	42.00	146.00	17
SPS-Zn	61.80	74.80	25.00	18
P(SBMA-co-AA)/Zn(CF ₃ SO ₃) ₂	22.40	35.70	27.60	19
p(CBMA-co-HEMA)	81.10	281.10	1.31	20

Table S2 R_s and R_{ct} parameters of ZHSC obtained from the Nyquist plot fitting.

Sample	R_s (Ω)	R_{ct} (Ω)
CH-ZHSC	10.6	5.9
CBH-ZHSC	4.0	4.1
Before	4.6	4.9
After	4.0	4.1

Table S3 Comparison of the electrochemical performance of the CBH-ZHSC in this work with other reported energy storage devices based on different types of electrolytes.

Hydrogel electrolyte	Type	Maximum energy density (Wh kg ⁻¹)	Maximum power density (W kg ⁻¹)	Cycling stability	Refs.
CBH-Zn	HE	97.4	16000.0	45000, 94%	This work
PAM/ZnSO ₄	HE	29.2	926.7	2000, 81.4%	21
Gelatin/ZnSO ₄	HE	86.8	12100.0	6500, 81.3%	22
PAM-co-PAA/-CG/ZnSO ₄	HE	54.9	3676.9	10000, 96.4%	23
PVA-CMC/Zn(CF ₃ SO ₃) ₂	HE	87.9	7727.5	10000, 84.8%	24
CG/PAM/Zn(CF ₃ SO ₃) ₂	HE	86.5	14900.0	10000, 102.7%	12
PVA/H ₃ PO ₄	HE	41.0	2800.0	200, 60.0%	25
PAM/CMC/XG/Zn(CF ₃ SO ₃) ₂	HE	96.8	15752.4	10000, 93.5%	26
CS-PAM/PA	HE	14.6	2310.2	10000, 97.5%	27
B-PVA/KCl/GO	HE	5.4	993.9	5000, 92%	28
PVA/(NH ₄) ₂ SO ₄	HE	18.4	18687.9	10000, 97.4%	29
PCA-CMC-LC	OHE	24.3	2167.9	10000, 75.0%	30
PVA DN/EG/H ₂ SO ₄	OHE	16.1	1717.3	—	31
F-MMT/PVA	OHE	26.2 mWh cm ⁻³	391.7 mW cm ⁻³	10000, 91.0%	32
ZnSO ₄	AE	84.0	14900.0	10000, 91.0%	33
ZnSO ₄	AE	102.2	12740.1	12000, 80.6%	34
Zn(CF ₃ SO ₃) ₂	AE	53.6	2291.5	2000, 98%	35
Zn(ClO ₄) ₂	AE	78.4	15691.8	30000, 99.2%	36
Zn (CF ₃ SO ₃) ₂	AE	67.2	15400.0	20000, 97.4%	37

Table S4 Composition of different samples.

Sample	Cellulose (g)	Alkaline solution (g)	Bentonite (g)	ZnSO ₄ concentration (mol L ⁻¹)
Cellulose hydrogel	3.0	97.0	0.0	0.0
Cellulose/BT hydrogel	3.0	97.0	0.3	0.0
CH-Zn	3.0	97.0	0.0	2.0
CBH-Zn	3.0	97.0	0.3	2.0

Section S8 References

- 1 Z. Li, L. Zhong, T. Zhang, F. Qiu, X. Yue and D. Yang, *ACS Sustain. Chem. Eng.*, 2019, **7**, 9984-9994.
- 2 L. Hu, Y. Zhong, S. Wu, P. Wei, J. Huang, D. Xu, L. Zhang, Q. Ye and J. Cai, *Chem. Eng. J.*, 2021, **417**, 129229.
- 3 F. Yue, Z. Tie, S. Deng, S. Wang, M. Yang and Z. Niu, *Angew. Chemie., Int. Ed.*, 2021, **60**, 13882-13886.
- 4 M. Chen, J. Chen, W. Zhou, J. Xu and C. Wong, *J. Mater. Chem. A*, 2019, **7**, 26524-26532.
- 5 Q. Fu, S. Hao, L. Meng, F. Xu and J. Yang, *ACS Nano*, 2021, **15**, 18469-18482.
- 6 B. Wang, J. Li, C. Hou, Q. Zhang, Y. Li and H. Wang, *ACS Appl. Mater. Interfaces*, 2020, **12**, 46005-46014.
- 7 L. Yang, L. Song, Y. Feng, M. Cao, P. Zhang, X. Zhang and J. Yao, *J. Mater. Chem. A*, 2020, **8**, 12314-12318.
- 8 Y. Quan, W. Zhou, T. Wu, M. Chen, X. Han, Q. Tian, J. Xu and J. Chen, *Chem. Eng. J.*, 2022, **446**, 137056.
- 9 W. Xu, C. Liu, Q. Wu, W. Xie, W. Kim, S. Lee and J. Gwon, *J. Mater. Chem. A*, 2020, **8**, 18327-18337.
- 10 H. Zhang, W. Niu and S. Zhang, *Chem. Eng. J.*, 2020, **387**, 124105.
- 11 H. Huang, L. Han, X. Fu, Y. Wang, Z. Yang, L. Pan and M. Xu, *Small*, 2021, **17**, 2006807.
- 12 D. Wu, C. Ji, H. Mi, F. Guo, H. Cui, P. Qiu and N. Yang, *Nanoscale*, 2021, **13**, 15869-15881.
- 13 J. Zhao, J. Gong, G. Wang, K. Zhu, K. Ye, J. Yan and D. Cao, *Chem. Eng. J.*, 2020, **401**, 125456.
- 14 T. Liu, S. Sutarsis, X. Zhong, W. Lin, S. Chou, N. Kirana, P. Huang, Y. Lo, J. Chang, P. Wu and S. Chen, *Energy Storage Mater.*, 2021, **38**, 489-498.
- 15 J. Nan, G. Zhang, T. Zhu, Z. Wang, L. Wang, H. Wang, F. Chu, C. Wang and C. Tang, *Adv. Sci.*, 2020, **7**, 2000587.

- 16 Y. Zhang, Y. Dai, F. Xia and X. Zhang, *Nano Energy*, 2022, **104**, 107977.
- 17 J. Yang, Z. Xu, J. Wang, L. Gai, X. Ji, H. Jiang and L. Liu, *Adv. Funct. Mater.*, 2021, **31**, 2009438.
- 18 T. Wu, C. Ji, H. Mi, F. Guo, G. Guo, B. Zhang and M. Wu, *J. Mater. Chem. A*, 2022, DOI: 10.1039/d2ta07410a.
- 19 X. Zhu, F. Guo, C. Ji, H. Mi, C. Liu and J. Qiu, *J. Mater. Chem. A*, 2022, **10**, 12856-12868.
- 20 X. Hu, P. Zhang, J. Liu, H. Guan, R. Xie, L. Cai, J. Guo, L. Wang, Y. Tian and X. Qiu, *Chem. Eng. J.*, 2022, **446**, 136988.
- 21 G. Lou, G. Pei, Y. Wu, Y. Lu, Y. Wu, X. Zhu, Y. Pang, Z. Shen, Q. Wu, S. Fu and H. Chen, *Chem. Eng. J.*, 2021, **413**, 127502.
- 22 Y. Lu, Z. Li, Z. Bai, H. Mi, C. Ji, H. Pang, C. Yu and J. Qiu, *Nano Energy*, 2019, **66**, 104132.
- 23 H. Cui, H. Mi, C. Ji, F. Guo, Y. Chen, D. Wu, J. Qiu and H. Xie, *J. Mater. Chem. A*, 2021, **9**, 23941-23954.
- 24 X. Zhu, C. Ji, Q. Meng, H. Mi, Q. Yang, Z. Li, N. Yang and J. Qiu, *Small*, 2022, **18**, 2200055.
- 25 S. Dai, W. Xu, Y. Xi, M. Wang, X. Gu, D. Guo and C. Hu, *Nano Energy*, 2016, **19**, 363-372.
- 26 J. Gao, F. Guo, C. Ji, X. He, H. Mi and J. Qiu, *J. Mater. Chem. A*, 2022, **10**, 24639-24648.
- 27 J. Xu, R. Jin, X. Ren and G. Gao, *Chem. Eng. J.*, 2021, **413**, 127446.
- 28 H. Peng, Y. Lv, G. Wei, J. Zhou, X. Gao, K. Sun, G. Ma and Z. Lei, *J. Power Sources*, 2019, **431**, 210-219.
- 29 J. Wei and Q. Wang, *Small Methods*, 2019, **3**, 1900558.
- 30 Y. Yang, K. Wang, Q. Zang, Q. Shi, Y. Wang, Z. Xiao, Q. Zhang and L. Wang, *J. Mater. Chem. A*, 2022, **10**, 11277-11287.
- 31 Z. Liu, J. Zhang, J. Liu, Y. Long, L. Fang, Q. Wang and T. Liu, *J. Mater. Chem. A*, 2020, **8**, 6219-6228.

- 32 Q. Liu, A. Zhao, X. He, Q. Li, J. Sun, Z. Lei and Z. H. Liu, *Adv. Funct. Mater.*, 2021, **31**, 2010944.
- 33 L. Dong, X. Ma, Y. Li, L. Zhao, W. Liu, J. Cheng, C. Xu, B. Li, Q. Yang and F. Kang, *Energy Storage Mater.*, 2018, **13**, 96-102.
- 34 J. Li, J. Zhang, L. Yu, J. Gao, X. He, H. Liu, Y. Guo and G. Zhang, *Energy Storage Mater.*, 2021, **42**, 705-714.
- 35 F. Li, Y. Liu, G. Wang, S. Zhang, D. Zhao, K. Fang, H. Zhang and H. Y. Yang, *Chem. Eng. J.*, 2022, **435**, 135052.
- 36 J. Yin, W. Zhang, W. Wang, N. A. Alhebshi, N. Salah and H. N. Alshareef, *Adv. Energy Mater.*, 2020, **10**, 2001705.
- 37 F. Wei, Y. Wei, J. Wang, M. Han and Y. Lv, *Chem. Eng. J.*, 2022, **450**, 137919.